

## LINE-NARROWING APPROACHES TO SOLID STATE NMR IMAGING

J. B. Miller, D. G. Cory\* and A. N. Garroway

Code 6122, Naval Research Laboratory, Washington, D. C. 20375-5000 USA

## Introduction

The fundamentals of magnetic resonance imaging (MRI) are well-established in the medical area. Extension of these ideas to materials sciences lags for a number of reasons: (i) medical sciences predominate materials sciences (health care accounts for 11% of the U.S. gross national product); (ii) despite some evocative demonstrations, imaging has not yet found proven applications in materials science (iii) the RF techniques required for solid state imaging are more complicated and not yet fully developed, especially for materials with very little internal molecular motion. We address item (iii).

For those materials which exhibit sufficient molecular motion to reduce magnetic dipolar couplings, the familiar techniques of medical MRI are appropriate, though perhaps with modifications to accommodate  $T_2$ 's down to the order of 1 ms. In comparison, the proton rigid lattice  $T_2$  value for a high protonated organic solid is of the order of 15-20  $\mu$ s. Line-narrowing methods, specialized to imaging, have met with some success in the general case of these less mobile materials (1-6).

We present here three topics: proton and carbon imaging; surface coil imaging with line narrowing; and determination of size distributions using restricted diffusion.

## Proton and Carbon Imaging

To image a solid, one must confront the line-broadening mechanisms which degrade resolution and sensitivity. For many systems, the greatest source of broadening is the dipolar coupling. One approach (1,3) to imaging by reducing the homonuclear dipolar coupling is the use of various multiple-pulse line-narrowing sequences, such as MREV-8 (7). Figure 1a shows a two-dimensional  $^1\text{H}$  image of an annulus of neoprene rubber surrounding but off center from a cylinder of adamantane. The image was obtained by appending the MREV-8 line-narrowing sequence to a two-dimensional Fourier transform imaging scheme. Pulse sequence details and a contour plot version of Fig. 1 appear in ref. [3]. The adamantane and neoprene were chosen for their different mobilities. By simple variations in

experimental parameters, we could alternatively suppress the more mobile neoprene or less mobile adamantane by rotating frame or laboratory frame discrimination, Fig 1b-c.

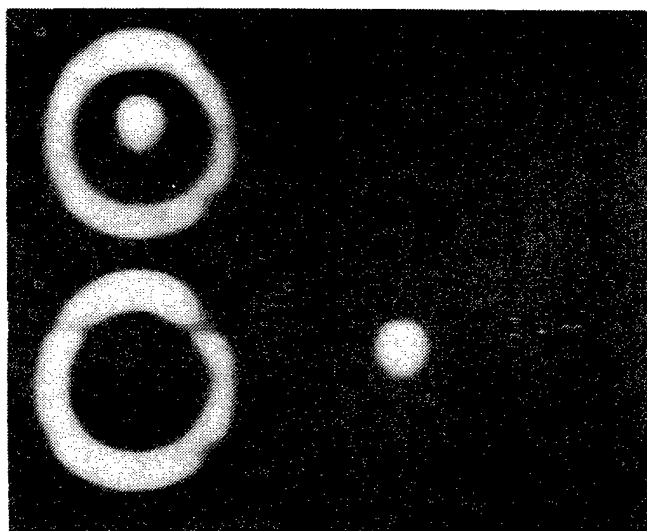


Fig. 1  $^1\text{H}$  solid state Fourier transform NMR images at 60 MHz of a neoprene rubber annulus surrounding an adamantane cylinder. The MREV-8 sequence was used to suppress dipolar broadening. The molecular mobilities are easily discriminated by  $T_1$  weighting (b) or  $T_{1\rho}$  weighting (c); there is no weighting in (a).

Adamantane was chosen, not because of its somewhat reduced dipolar coupling, but because there is no chemical shift anisotropy, the differences in isotropic chemical shift are small, and the static bulk susceptibility is reasonably small. It is a characteristic of the two-dimensional Fourier transform techniques with a first interval of fixed length that in the second ( $t_2$ ) interval, the image is convoluted by broadening terms linear in the spin operator  $I_z$ . We can remove such inhomogeneous broadening by, in the simplest case, creating echoes by a Carr-Purcell-Meiboom-Gill (CPMG) sequence (8) which is synchronous with an oscillating gradient (9,10). We have termed this Refocused

Gradient Imaging (RGI), as the line broadening effects are refocused at the time of the echo, while the echoes are frequency encoded by the gradient.

For carbon RGI (11), use of a CPMG sequence is adequate, with the addition of cross-polarization and proton decoupling. For non-interacting spins, one may think of the CPMG sequence as reversing the effective field from  $+z$  to  $-z$  from one echo to the next, so that the magnetization appears to precess first positively and then negatively about the  $z$  axis. The situation is more delicate for proton imaging since the proton homonuclear coupling must be removed. For the MREV-8 sequence, the magnetization precesses about the  $(-1,0,1)$  axis, for a particular choice of rf phases. Implementing the analogous refocused imaging strategy for the MREV-8 sequence is more complicated. The sequence chosen (12) switches the effective field along the  $+(-3,0,2)$  direction. Figure 2 shows proton and carbon RGI images for the same specimen, a polyacrylic polymer of dimensions  $4.5 \times 5.5 \times 16$  mm. A notch was cut parallel to the long direction in one of the  $4.5 \times 16$  mm faces. Back projection was used for both images: 18 projections were obtained at  $10^\circ$  intervals. For the proton image, about 40 minutes of data taking were required; for the carbon image, 10 hours. Despite the weaker carbon signal, the notch feature is clearly seen in image of Fig. 2b.

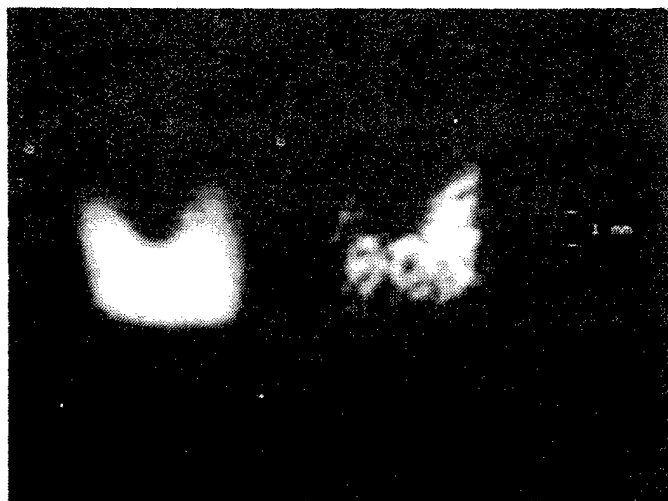


Fig. 2  $^1\text{H}$  and  $^{13}\text{C}$  images of a polyacrylic specimen, at 100 and 25 MHz, respectively. A notch was cut into one face as shown in the inset. Refocused gradient imaging was used for each, to remove inhomogeneous broadening. The images were obtained by back projection (18 projections) and without slice selection.

Heteronuclear line narrowing is technically much easier than homonuclear narrowing and the sacrifice in the signal-to-noise ratio on comparing (11,13) carbon imaging with proton imaging is somewhat less drastic than predicted just from a comparison of the respective spectroscopies. We estimate (11) that for our representative experimental conditions, the relative sensitivity of carbon to proton RGI is about  $7.6 \times 10^{-3}$ , about 40 times larger than the ratio determined just by the receptivity of  $1.8 \times 10^{-4}$  which would be applicable for a comparison of spectroscopy rather than imaging.

We find that solid state imaging by dipolar decoupling sequences is substantially improved by the refocused gradient approach which further removes isotropic and anisotropic chemical shifts, susceptibilities and background gradients, as illustrated both for protons and carbon.

### Surface Coil Imaging

One easily imagines samples which are too large to fit into the RF coil. Here one can use the variation of the RF field to profile the spin density in, say, the  $z$  direction. Variations in  $x$  and  $y$  may be insignificant or perhaps accommodated by manually moving the surface coil. The prototypical geometry is a very large, thin sheet of material. We wish to use the surface coil for both excitation and detection and, also, to allow the possibility of recording spatial variations in chemistry, so that the chemical shift data are preserved.

Our approach (14,15) to solid state surface coil imaging is to break the problem into two parts: selecting a region, a more-or-less planar surface, and prolonging the signal to improved signal-to-noise. For the latter we have used the MREV-8 sequence or pulsed spin-locking, depending on whether chemical shift information is desired. For the selectivity, we have used a simple train of  $\theta$  pulses, separated by a time longer than  $T_2$ . Those spins which see a multiple of a  $\pi$  rotation will remain along  $z$  while all other spins will dephase. A train of  $n\theta$  pulses selects a region described by  $\cos^n(\theta)$ .

For liquids imaging, this selectivity can be improved by using the Shaka-Freeman (16) sequence,  $(\pi - 2\pi - 3\pi - \dots - n\pi)_2$ . For protonated solids, the dipolar coupling operates during these pulses, albeit at half strength. Accordingly, after even a small number of these inversion pulses, the magnetization decays by dipolar dephasing.

We have addressed this latter issue by substituting dipolar decoupled composite inversion pulse (DDCIP) for the  $\pi$  pulses in the Shaka-Freeman sequence. Of the possible implementations

of DDCIP, we use [+X +Y -X -X -Y -X], where X represents a  $\pi/2$  RF pulse along the x axis. On comparing a Shaka-Freeman sequence made up with  $\pi$  pulses to one made with DDCIP, we find (15) an order of magnitude more longitudinal magnetization remains after 20 inverting pulses.

A one-dimensional profile of a polyacrylic/Teflon sandwich is shown in Fig. 3, using DDCIP in a Shaka-Freeman sequence. In this particular case we used pulsed spin-lock detection. The polyacrylic plates are 8 x 8 x 1.2 mm with 1.0 mm Teflon spacers. Near the coil, resolution in this proton image is better than 200  $\mu\text{m}$ .

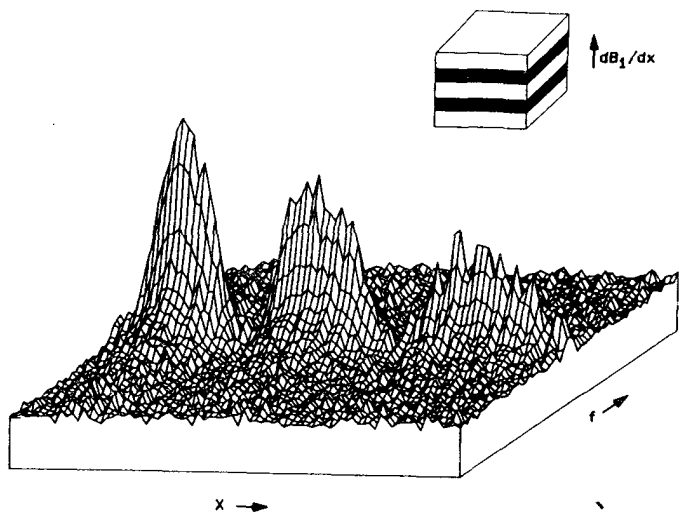


Fig. 3 One-dimensional surface coil  $^1\text{H}$  image of a polyacrylic/Teflon sandwich (inset). A dipolar decoupled composite inversion pulse was used in a Shaka-Freeman spatially selective pulse sequence. Transmitter power was stepped along one axis to look further into the sample. The second dimension is the Fourier transform of the pulsed spin-lock data: alternatively, pulsed spin-lock detection could be replaced by an MREV-8 sequence to allow for spatially varying chemical shift.

### Spatial Distributions

Consider a sample which contains many small features: small structures, defects, granules, compartments, cells, *et cetera*. The overall shape of the specimen is unimportant, as are the details of the locations of each of these small structures. What is desired is the size distribution of these structures. This idealized case is more appropriate to materials science than conventional MRI applications.

One approach (17) is to create a full three-dimensional image and then image analyze to tabulate the size of each defect. Such a method, though feasible, is very tedious and, more importantly, requires that each and every structure contribute enough signal to be separately resolvable. In this approach, signal-to-noise ratio is the overriding factor in limiting resolution. This limitation is not immutable, as we show.

It would be most elegant to generate this size distribution of these small structures directly, without the requirement to resolve each voxel. In such a display each structure is centered at some arbitrary zero point, rather than dispersed at its absolute coordinates within the sample. The projection of such a relative displacement image onto the position axis would give the size distribution of these defects. Since all these  $n$  defects contribute to the relative displacement image, the signal-to-noise ratio would increase by  $n$ . For regular or partly disordered samples, such an approach is possible (18). For disordered samples, we are not aware of any general solution.

We look for a way to illuminate by NMR only the size of these small structures while suppressing their absolute positions. A less-than-general approach is to examine specimens which demonstrate restricted (or bounded) diffusion in which the spins freely diffuse until they are reflected at the walls of restricting cells. The idea is to use these mobile spins to report the dimensions rather than the positions of their compartments. Indeed the compartment dimensions are defined by the ability to reflect spins at its boundaries. Restricted diffusion has been studied earlier by Stejskal and Tanner (19) by the pulsed gradient spin echo method (20). This method customarily uses fixed gradient strengths and examines the echo decay (either of the Hahn echo or the stimulated echo) as a function of delay between gradient pulses. The analysis (21,22) is more straightforward when the timing is held constant and the gradient amplitude is incremented, as in Fig. 5a.

For the stimulated echo sequence, provided diffusion during the gradient pulse can be neglected in comparison to diffusion between gradient pulses, the echo attenuation is:

$$S(g) = \iint \rho(r_0) P(r_0; r, t_d) X \exp [i\gamma t_e g \cdot (r - r_0)] dr dr_0 \quad [1]$$

where  $\rho(r_0)$  is the density as a function of initial position  $r_0$ , during the first gradient pulse;  $P(r_0; r, t_d)$  is the conditional probability that a spin initially at  $r_0$  will diffuse to  $r$  after a time  $t_d$ ;  $t_e$  is the encoding time defined by the duration of the gradient pulse; and  $g$  is the gradient field strength which is stepped in

equal increments during the experiment.

If we were to remove the second gradient pulse in Fig. 5a, we should have a rudimentary one-dimensional phase encoding imaging sequence, giving the absolute position of all the spins. As these spins are distributed essentially randomly, we should see only a uniform spin density  $\rho(r_0)$ . But with the second gradient we refocus all spins which have not moved and phase encode the relative displacement  $r-r_0$ .

Consider a relative displacement  $x$  along the gradient direction. Fourier transforming Eq. [1] against the variable  $\gamma t_e g$ , we have

$$I(x) = \text{F.T.}\{S(g)\} \\ = \int \rho(r_0) P(r_0; r_0 + x, t_d) dr_0. \quad [2]$$

The advantage of stepping the gradient is seen from Eq. [2]; the Fourier transform of the echo  $S(g)$  directly gives the conditional probability for the relative displacement  $x$ . We have removed the absolute position information and record only relative displacement. This is an important step towards measuring small spatial features, as we now examine.

Look over sufficiently long time: the Gaussian describing the initial free diffusion dies out and the conditional probability for displacement is determined by an ensemble average of the various displacements available to the spin. Displacements taking the spin outside the restricting structure are not allowed. The walls are presumed to be perfectly reflecting. In this long term, the allowable displacements are determined simply by the shape,  $\zeta(r)$ , of the restriction:

$$P(r_0; r_0 + x, t_d) = \zeta(r_0 + x), \quad [3]$$

where  $\rho(r_0) = c \zeta(r_0)$ . Hence the echo amplitude for the pulsed gradient response is, for restricted one-dimensional diffusion,

$$S(g) = c \int \int \zeta(r_0) \zeta(r_0 + x) \\ X \exp(i\gamma t_e g x) dx dr_0. \quad [4]$$

Thus the echo signal in the  $k$ -space domain ( $k = \gamma g t_d$ ) is the Fourier transform of the shape autocorrelation function. Furthermore, since convolution in one domain is equivalent to multiplication in the conjugate domain, we see that the Fourier transform of the echo response,  $S(g)$ , is just the power spectrum of the shape function:

$$I(x) = \text{F.T.}\{S(g)\} \\ = c [\text{F.T.}\{\zeta(x)\}]^2. \quad [5]$$

For example, a rectangular shape function

of width  $L$  has a triangular autocorrelation function  $[1 - |(x/L)|]$ . An optical analogy to the echo response is the power diffraction pattern of a single slit, or the amplitude diffraction pattern from a slit whose transmission varies in a triangular manner.

We can take this optical analogy further, as in Fig. 4. Consider the resulting interference pattern for a planar  $N$ -slit grating in which the slit widths are uniform but the slit spacings are random. Illumination is even. For  $N$  large, due to destructive interference the resulting interference pattern will have many weak peaks but no strong peaks. This situation is perfectly analogous to a one-dimensional NMR image of a one-dimensional random array of cells of uniform widths: each cell must be individually resolved. In contrast for the restricted diffusion case, we essentially collapse the multiple-slit grating into a single slit. We retain the

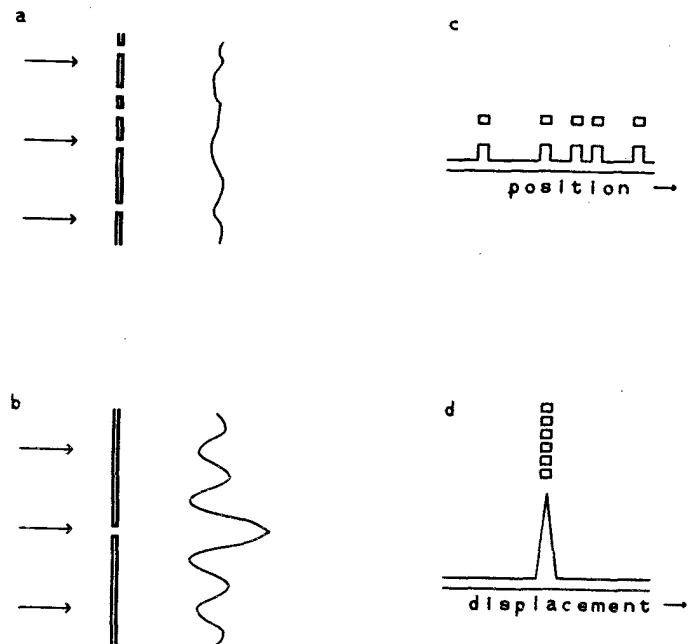


Fig. 4 One-dimensional optical analogy of restricted diffusion. In (a) is a multiple-slit grating; slit widths are constant, but spacings are random. In (b) is a single slit. The (far field) amplitude diffraction patterns for each are indicated schematically. In (c) is a specimen of small cells of uniform width and arbitrary position; the corresponding one-dimensional NMR projection is indicated. In (d) the cells have been shifted to a common origin and the displacement probability is determined by the pulse sequence of Fig. 5a as the spins execute restricted diffusion within the cells. Case (d) is analogous to converting the multiple-slit interference pattern (b) into a single-slit diffraction pattern (a).

single-slit diffraction pattern, conveying the width of each slit, and remove the interference pattern arising from the absolute position of each slit. Furthermore, the resulting single-slit diffraction pattern is  $N$  times more intense in amplitude. Though we illustrate the optical analogy in one dimension, it is easily extended to higher dimensions.

The optical analogy to the NMR treatment of restricted diffusion is almost perfect, except that we do not see the shape function (slit width) directly, but rather the autocorrelation of the shape function. We do not know a general way to recover uniquely the shape function from its autocorrelation function. This difficulty arises from our loss of

'phase' information: in the Fourier response of Eq. [5] we have the power spectrum, but would prefer the amplitude spectrum to find the shape function (or distribution of shape functions) directly. A further complication arises if there is a distribution of sizes; the size distribution function will convolve with the shape autocorrelation function, making it difficult to separate the shape function from the size distribution function. For example, the following situations give the same echo response: (i) a specimen of uniform spheres and (ii) a collection of one-dimensional cells whose size distribution function infelicitously approximates a spherical weighting function.

Even though the size distribution function cannot be determined uniquely, one may appeal to a particular model or, at the very least, infer the characteristic size of the restrictions directly from the displacement profile,  $I(x)$ . We determined the translational displacement probability for restricted diffusion of water in yeast cells by the pulse sequence of Fig. 5a. Results, Fig. 5b, indicate a characteristic cell width of about  $5 \mu\text{m}$ ; recall that spins in a box of width  $L$  can diffuse from  $-L$  to  $+L$ . For NMR microscopy one estimate (23) of the minimum resolvable voxel is the order of  $(10 \mu\text{m})^3$  for protons in a liquid-like sample at 600 MHz. In our case, spatial resolution is determined by the rather modest gradient (1.0 T/m; 100 G/cm) available, rather than by signal-to-noise: in our experiment all the yeast cells in the sample contribute intensity in a very narrow region of the displacement image.

### Conclusions

We have demonstrated some approaches to solid state imaging by line-narrowing methods both for rare (carbon) and abundant (proton) spin species. In addition to the dipolar couplings, we have demonstrated that chemical shift-like broadening can be removed. Surface coil imaging is attractive for those sample geometries which cannot be accommodated in an RF coil. Finally, as a step towards determining random small scale structure in solids, we have treated the less general case of restricted diffusion and showed that structural features far smaller than those resolvable by NMR imaging microscopy can be examined.

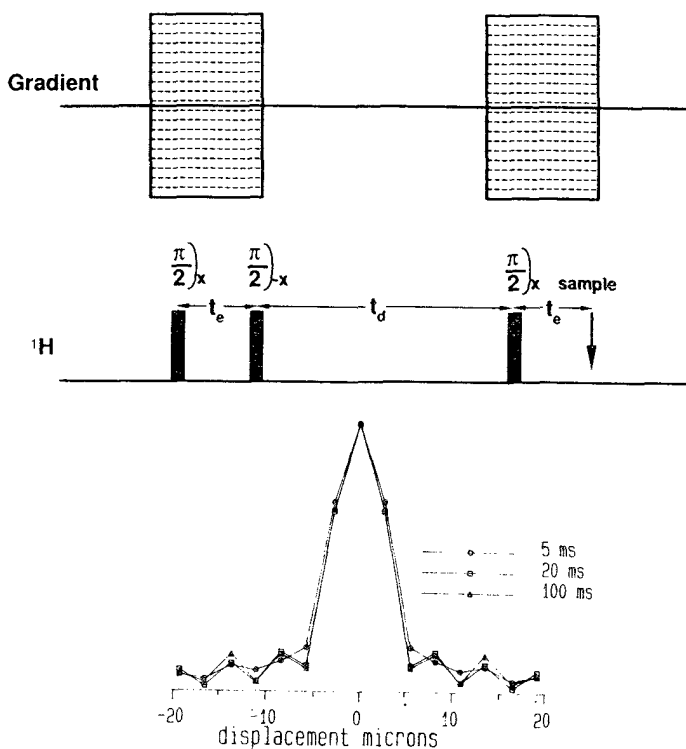


Fig. 5 (a) Pulse sequence for determining conditional translational probabilities and (b) displacement profiles for water in yeast cells at three different values of evolution time,  $t_e$ . The stimulated echo pulsed gradient sequence is modified: the gradient strength is incremented while the pulse timing remains fixed. The echo amplitude is Fourier transformed with the gradient strength as the variable. The diffusion of water in yeast cells is restricted over time scales longer than about 5 ms. From (b) the characteristic cell size is about  $5 \mu\text{m}$ .

## Footnotes and References

\* National Research Council/ Naval Research Laboratory postdoctoral associate.

1. (a) P. Mansfield, P. K. Grannell, A. N. Garroway, and D.C. Stalker, Proceedings, 1st Spec. Colloque Ampere, edited by J. W. Hennel (Krakow, 1973), p. 16; (b) P. Mansfield and P. K. Grannell, J. Phys. C. 6, L422 (1973).
2. R. A. Wind and C. S. Yannoni, J. Magn. Reson. **36**, 269 (1979).
3. G. C. Chingas, J. B. Miller, and A. N. Garroway, J. Magn. Reson. **66**, 530 (1986).
4. F. DeLuca, C. Nuccetelli, B. C. De Simone, and B. Maraviglia, J. Magn. Reson. **69**, 496 (1986).
5. D. G. Cory, A. M. Reichwein, J. W. M. van Os and W. S. Veeman, Chem. Phys. Lett. **143**, 467 (1988).
6. J. B. Miller and A. N. Garroway, J. Magn. Reson. **82**, 529 (1989).
- 7.(a) P. Mansfield, J. Phys. C **4**, 1444 (1971), (b) W. -K. Rhim, D. D. Elleman, and R. W. Vaughan, J. Chem. Phys. **58**, 1772 (1973), (c) W. -K. Rhim, D. D. Elleman, and R. W. Vaughan, J. Chem. Phys. **59**, 3740 (1973).
8. S. Meiboom and D. Gill, Rev. Sci. Instrum. **29**, 688 (1958).
9. P. Bendel, IEEE Trans. Med. Imaging **MI-4**, 114 (1985).
10. J. B. Miller and A. N. Garroway, J. Magn. Reson. **67**, 575 (1986).
11. J. B. Miller and A. N. Garroway, J. Magn. Reson. in press.
12. J. B. Miller and A. N. Garroway, J. Magn. Reson. **82**, 529 (1989).
13. D. G. Cory and W. S. Veeman, J. Phys. E, Sci. Instrum. **22**, 180 (1989).
14. J. B. Miller and A. N. Garroway, J. Magn. Reson. **77**, 187 (1988).
15. J. B. Miller and A. N. Garroway, J. Magn. Reson. submitted.
16. A. J. Shaka and R. Freeman, J. Magn. Reson. **64**, 145 (1985).
17. D. W. Kormos (private communication, 1989).
18. P. Mansfield and P. K. Grannell, Phys. Rev. B **12**, 3618 (1975).
19. J. E. Tanner and E. O. Stejskal, J. Chem. Phys. **49**, 1768 (1968).
20. E. O. Stejskal, J. Chem. Phys. **43**, 3597 (1965)
21. D. G. Cory and A. N. Garroway, Mag. Reson. in Med., in press.
22. (a) J. Kärger, H. Pfeifer and W. Heink, Advances in Magnetic Resonance, vol. 12, ed. J. S. Waugh (Academic Press, San Diego) p. 1, 1988, (b) P. T. Callaghan, Aust. J. Phys. **37**, 359 (1984).
23. P. Mansfield and P. C. Morris, "Advances in Magnetic Resonance," Supp. 2, NMR Imaging in Biomedicine, p.198 (Academic Press, New York, 1982).